

Development and Experimental Validation of a Non-Linear, All-Elastomer In-Plane Capacitive Pressure Sensor Model

Kourosh M. Kalayeh, Alexi Charalambides, Sarah Bergbreiter, and Panos G. Charalambides

Abstract—A large deformation mechanics model is applied to predict capacitance changes in an all-elastomer capacitive tactile sensor, and the predictive model is experimentally validated. The compressive model predicts a non-linear relationship between the contact normal force and resulting capacitance change due to changes in electrode gap and electrode layer thickness. Broad parametric studies demonstrate that higher sensitivities can be achieved with lower modulus materials and smaller electrode gaps. Sensors are fabricated using a reusable silicon mold and experimental results are compared to predictions from the capacitance model. Capacitance-force model predictions yielded by the calibrated capacitance analytical model are shown to be in remarkable agreement with experimental measurements. A fringe effects term included in the capacitance model highlights the limitations of the parallel plate model especially for sensors with large electrode layer gaps.

Index Terms—Capacitive tactile sensor, experiments, experimental validation, microfabrication, non-linear predictive model, optimal sensor design, parametric studies.

I. INTRODUCTION

TACTILE sensing in robots has been a topic of growing interest due to the need for increased dexterity to interact safely and precisely with humans and other objects [1]–[4]. Effective grasping of soft objects, including people, in home-care or medical contexts requires knowledge of the forces that the robot is applying to the object [5]. Safe interaction between humans and robots working together on manufacturing tasks also requires better knowledge of contact and proximity [6], [7]. Soft sensors can make interaction safer, but knowledge of contact and applied forces can be improved through the use of large arrays of small sensors along with a model that can predict contact forces. The goal of this work is to provide both a novel, low-cost sensor design as well as a non-linear model that help design and predict the outputs of this sensor. It may be of importance to note that the research presented

in this work focuses only on the static sensor response. While important, the dynamic sensor response is beyond the scope of this paper and shall be addressed in future studies.

Microfabrication offers the opportunity to take advantage of batch fabrication and high spatial resolution (< 1 sensors/mm²). However, soft, stretchable and/or flexible arrays of tactile sensors usually require the use of polymers (elastomers are particularly common), fibers, or foams that are not common to microfabrication. As such, many sensors take advantage of metals and more rigid polymers (modulus ≈ 1 GPa). Kim used traditional metal strain gauges embedded in a polyimide and silicone elastomer matrix to achieve sensor densities of 1 sensor/mm² with included wiring and interconnects [8]. Significant work takes advantage of the piezoresistive properties of conductive polymers that undergo large changes in resistance when strained [9] and these sensors have even been commercialized through companies like TekScan [10]. Elastomer composites made from mixing conductive particles into an elastomer were used by Strohmayer with crossed metal wires to create a pressure-sensitive resistance between the wires [11]. Ventrelli created tactile skins using home-made conductive elastomer composites made from carbon black mixed with polydimethylsiloxane (PDMS) and found good results, but significant hysteresis [12]. These hysteresis results match our own preliminary work in mixing carbon black with PDMS [13]. One method to combat hysteresis in resistive sensors has been the use of liquid metal in microchannels [14]. However, these sensors are still quite large (sensor/cm²).

It is clear that conductive polymers can provide significant benefits to tactile sensing; they are easy to use, soft, conformable, and robust. In [15], Boie presented a novel capacitive tactile sensor which has a three layer sandwiched structure on a flexible printed circuit board (FPCB) substrate. Capacitive sensing is a potential transduction approach that can avoid hysteresis seen in elastomer-based resistive sensing. Capacitive sensing is a common approach in many high density microfabricated tactile sensors but these are traditionally made from rigid materials like polysilicon [16], [17]. Relatively large capacitance sensors made from low-hysteresis foam dielectrics have shown excellent responses and use in collision detection for human-friendly robotics [7], [18]. These sensors use a conductive fabric for the electrodes so are not as elastic as a conductive polymer electrode might be. Metals like gold have also been used to provide electrodes in capacitive tactile sensors but are still relatively large (sensor/cm²) [19].

Manuscript received May 26, 2016; revised October 31, 2016; accepted November 8, 2016. Date of publication November 11, 2016; date of current version December 20, 2016. The work of A. Charalambides and S. Bergbreiter was supported by NASA under Award NNX12AM02G. The associate editor coordinating the review of this paper and approving it for publication was Prof. Paul C.-P. Chao. (*Kourosh M. Kalayeh and Alexi Charalambides are co-first authors.*)

K. M. Kalayeh and P. G. Charalambides are with the Department of Mechanical Engineering, University of Maryland, Baltimore County, Baltimore, MD 21250 USA (e-mail: panos@umbc.edu).

A. Charalambides and S. Bergbreiter are with the Department of Mechanical Engineering and the Institute for Systems Research, University of Maryland, College Park, MD 20742 USA (e-mail: sarahb@umd.edu).

Digital Object Identifier 10.1109/JSEN.2016.2628200

TABLE I
METRICS OF NOTABLE NORMAL FORCE TACTILE SENSORS

Publication	Type	Range	Resolution	Dynamic Range	Fabrication Complexity
Mannsfeld [30]	Capacitive	7 ^a kPa	3 Pa	2333:1	Medium
Bao [21]	Capacitive	1 MPA	50 kPa	20:1	Medium
Lee [20]	Capacitive	40 mN	4 ^a mN	10:1	High
Park [31]	Resistive	3.93 ^b N	1.18 ^b N	3.3:1	Medium
Fearing [32]	Capacitive	500 ^b mN	5 ^b mN	100:1	High
Howe [33]	Capacitive	2 N	1 mN	2000:1	Medium
This work	Capacitive	2000 mN	75 mN	26:1	Low

^a Value based on figure or plot within publication

^b Value calculated from metrics within publication

PDMS has been used with embedded metal electrodes to provide impressive 32×32 arrays of microfabricated sensors with densities under sensor/mm² [20].

Similar sensors have also been demonstrated by spraying or painting on networks of conductive nanoparticles [21]–[23]. These have typically been millimeters in size or larger. Another approach to create more elastic electrodes is to use liquid conductors made from alloys that remain liquid at room temperature [24]–[26]. While typically larger scale, capacitive sensors using liquid metal electrodes have been demonstrated at sub-millimeter size scales [24]. Finally, laser ablated conductive elastomer electrodes have been used to demonstrate capacitive touch sensing in [27].

While there are a large number of existing compliant sensors, including those with high spatial resolution, there is very little modeling work on these sensors. Modeling is particularly challenging as elastomeric materials in particular demonstrate very non-linear stress-strain responses. Several examples of soft sensor modeling studied the effect of channel shape in the liquid metal sensors mentioned previously [14], [26]. Capacitive sensor models are typically limited to strain sensing that does not require fixed boundary conditions that make pressure sensing even more complex [23], [25], [26]. This work addresses the lack of a large deformation mechanics model for elastomer-based pressure sensors and the model is experimentally validated with results obtained as part of this study. The new model expands the sensing range validated from first order models in [28] from 350 mN to over 1.5 N. The fabrication process used in [28] has also been improved to make use of a reusable silicon mold, similar to [29], to lower sensor costs. The primary contributions of this work include the description of a non-linear model that predicts performance in a generic class of both pressure and strain all-elastomer sensors as well as validation of this model on small-scale, all-elastomer pressure sensors. Table I compares the minimum resolution, the test range and the dynamic range(range:resolution) of the sensor designed and fabricated in this study with similar works in the literature as indicated.

II. SENSOR MODEL

A schematic of the developed in-plane sensor is shown in Fig. 1. A rectangular sensor geometry that undergoes a uniform compressive stress will compress in the direction of

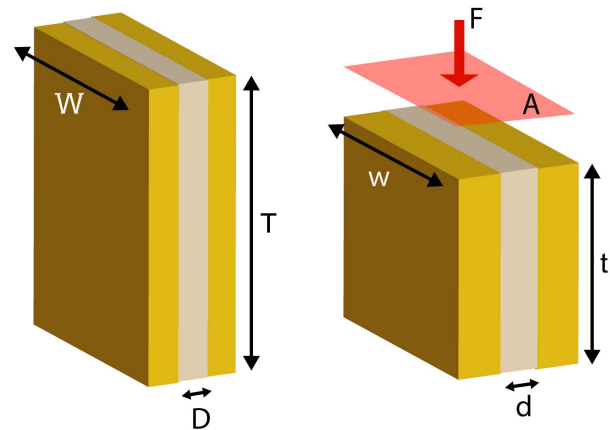


Fig. 1. An applied pressure compresses and expands the all-elastomer sensor through Poisson's effect, resulting in a decreased capacitance across the electrodes. The electrodes (color: gold) sandwich the dielectric (color: beige).

the applied force and expand perpendicularly to the applied force as governed by Poisson's ratio. Given the material properties, the deformation (and ultimately capacitance) can be related to the force and pressure applied. This physical phenomenon can be measured by placing compliant electrodes on either end of the deformed material, so that the deformation is correlated to a change in capacitance across the electrodes. To predict capacitance change with a given applied force, a large deformation, layer compression analytical model previously developed by the authors [34] is used to determine changes in sensor gap, length, and width.

This mechanics model is combined with a parallel plate capacitor model while also introducing a fringe effects term to determine a change in capacitance. A cross-sectional view of a complete sensor design is shown in Fig. 2(a), including top and bottom dielectric layers. Conductive elastomer electrodes are embedded into a soft elastomeric layer of initial thickness H . Upon contact, the soft polymeric layer compresses to a smaller thickness h while at the same time displacing material symmetrically outwards from the center of contact. Thus, the initial electrode spacing D increases to a larger spacing d while also the electrode layer thickness reduces from an initial thickness T to a current thickness t . Consistent with the flowchart included in Fig. 2(b), the capacitance C which is

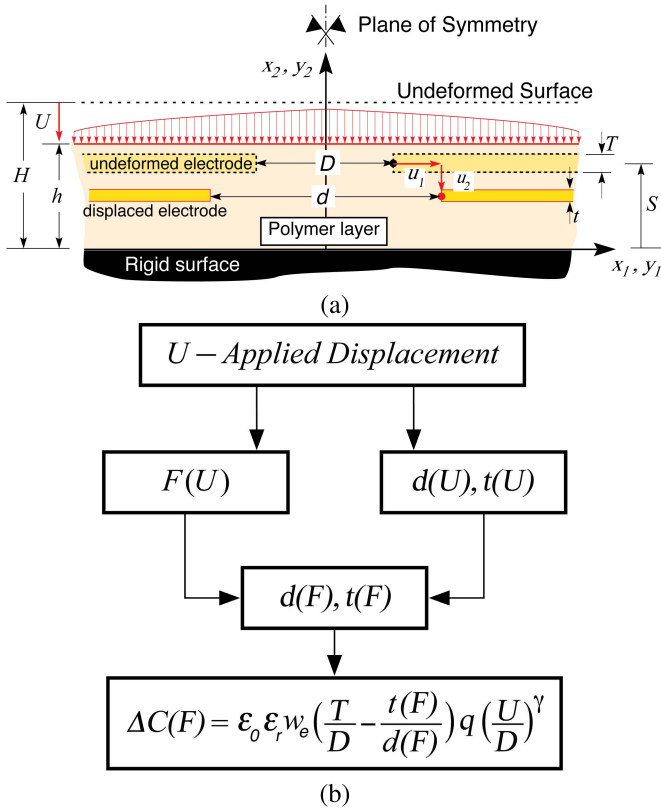


Fig. 2. (a) A cross-sectional view of the sensor designed and modeled in this study. (b) A flow chart indicating the process used to establish the relationship between the sensor capacitance $C(F)$ and the applied contact force F . The constants q and γ are determined through model calibration studies.

proportional to the electrode overlapping area A and inversely proportional to the current electrode distance d changes during contact. As will be discussed later on in this study, in addition to the parallel plate capacitance effects, the capacitance model included in Fig. 2(b) also accounts for fringe effects through the constants q and γ determined through the model comparisons to reported experimental capacitance change predictions.

A. The Large Deformation Layer Compression Model

The plane strain large deformation model developed in [34] was developed consistent with large deformation kinematics. Functional relations relating the deformed to the undeformed states were first employed. Material incompressibility was used along with a Mooney-Rivlin (M-R) constitutive model with the aid of which the Cauchy stresses were obtained as a function of the Finger deformation tensor, B [35]. The independent pressure term, P , appearing in the M-R model and derived in [34] takes the form,

$$P = C_2 x_1^2 f'^2 + \frac{(C_1 - C_2)}{2} A x_1^2 f^2 + \frac{(C_1 + C_2)}{2} \frac{1}{f^2} + C_2 f^2 + \Pi, \quad (1)$$

where C_1 and C_2 are the M-R material constants and A and Π are constants determined by enforcing local and global boundary conditions and depend on the layer compression level U/H . Again, a detailed presentation of the model can be found in [34].

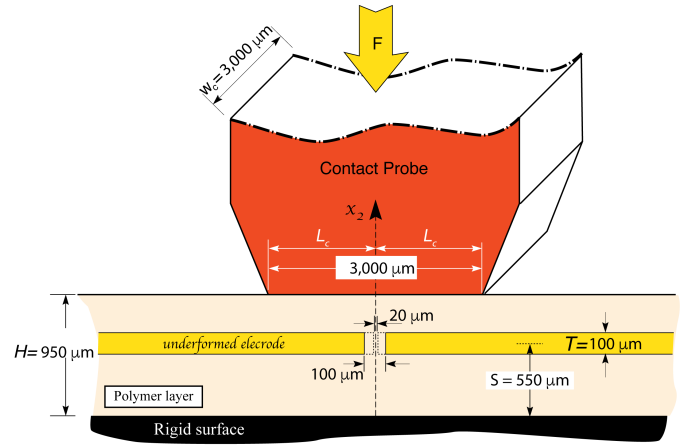


Fig. 3. A schematic showing the geometry of the MEMS pressure sensor fabricated and tested in this study. It may be of importance to note that the aspect ratio of the contact probe to electrode gap varies from a low of 30 for electrode gap of $100 \mu\text{m}$ to 150 for electrode gap of $20 \mu\text{m}$. In either case, the infinitely long layer model used in the development of the analytical model is justified since only the mechanics in the vicinity of the electrode gap is used in the capacitance model.

Small deformation, small strain theory applies to systems undergoing strains of the order of 0.001 leading to deformations that are of the order of $10^{-3} L_C$, where L_C represents a characteristic component dimension such as the height H of the sensor dielectric layer. The current large deformation, large strain non-linear model is capable of predicting the sensor response under severe layer compression of the order of $0.5H$ [34]. Under such large layer compression, strains of the order of 0.5, which is approximately three orders of magnitude larger than the typical small strain assumption. As will be seen later on in this study, the upper range of the capacitance force sensor response corresponds to approximately $U/H = 0.25$ resulting in large strains of the order of 0.25.

It may be of importance to state that the sensor developed herein was not tested while being stretched in directions orthogonal to the applied normal force as seen in the sensors with micro fluidic channels (eutectic Gallium Indium a.k.a eGaIn based sensors) [14], [31], however the sensors are qualitatively flexible and can be affixed to highly curved surfaces exposing the sensor to a large deformation environment.

B. Finding Force From Displacement

The model above predicts geometry changes within the elastomeric layer given a uniform displacement U . To determine forces applied in this tactile sensor, the relationship between the applied displacement U and the resulting contact pressure or associated contact force F needs to be established. This is done by integrating the Cauchy stress component σ_{22} presented in [34] over the contact area (force applied with a probe as seen in Fig. 3).

As shown in [34], the force-displacement expression for a total force acting over an undeformed contact area $2L_c \times w_c$ takes the form,

$$F = 2w_c L_c \lambda \left(-\frac{C_1 - C_2}{6} A L^2 \lambda^2 + \frac{C_1 - C_2}{2} \frac{1}{\lambda^2} - \Pi \right), \quad (2)$$

where C_1, C_2 are the M-R material constants, $\lambda = f(x_2 = H)$ is the principal stretch ratio for material points on the top surface of the polymer layer, w_c is the contact probe width, L_c is the contact probe half length as shown schematically in Fig. 3, and A and Π are constants determined through boundary and global equilibrium conditions and depend on the layer compression level U/H . The constant A is negative and is given as $A = -\alpha^2$, where α is obtained by solving a non-linear equation resulting from the geometric condition $g(x_2 = H) = h$.

The constant Π is calculated by enforcing global force equilibrium in the y_1 or x_1 directions as discussed in [34]. However, this calculation highlights an important consequence of the model in Sec. II-A; specifically, the bottom of this infinite layer is fixed and contact with the sensor will be realistically limited to a finite surface. An extensive discussion on enforcing force equilibrium to determine the constant Π from Eq. (2) is presented in [34]. In summary and with the aid of finite elements as discussed in [34], this equilibrium condition can be simplified to,

$$\int_0^h \sigma_{11}(y_1 = 0, y_2) dy_2 + \sigma_{12}^{max} L_s \left(\frac{U}{H} \right) = 0, \quad (3)$$

where,

$$\sigma_{12}^{max} = \sigma_{12}(x_1 = H, x_2 = 0) = \mu \alpha H \tan(\alpha H). \quad (4)$$

In the above expression, μ is the shear modulus, α is the model constant (which depends on (U/H)), and H is the sensor layer initial thickness. In this study, the effective length L_s which as indicated depends on the level of layer compression U/H is defined as follows,

$$L_s \left(\frac{U}{H} \right) = \zeta H \left(\frac{U}{H} \right)^m, \quad (5)$$

where, ζ and m represent constants controlling the effective length over which non-zero shear stresses developed at the bottom surface of the layer as discussed in [34]. As will become apparent later in this study, the latter constants are determined through model comparisons to experiments. Once ζ and m are found from experimental data, Eqs. (2)-(5) can be used to determine the force applied to the sensor from a probe with a known geometry given the normalized surface compression U/H .

C. Pressure Sensor Capacitance Estimates

The capacitance between two parallel plates is given by,

$$C = \epsilon_r \epsilon_0 \frac{t w_e}{d}, \quad (6)$$

where ϵ_0 and ϵ_r are the permittivity of free space and the relative permittivity of material between the plates respectively, t is the deformed height of the electrodes, w_e is the electrode width (consequently, $t w_e$ is the overlapping area between the plates) and d is the gap between the plates. While the above parallel plate model may provide good capacitance estimates for small electrode gaps, i.e., $d \ll t, w_e$, it may deviate appreciably as the electrode gap becomes comparable to the electrode dimensions [36], [37]. For sensors with such large

electrode gaps, the electric flux density fringe field may play an equally important role in controlling the sensor capacitance.

In light of the above, and based on the experimental results reported in [28] and herein and with the aid of the analytical model presented in [34], the parallel plate model is used as a springboard to develop a capacitance change model that accounts for both the parallel plate as well as the fringe field. More specifically, based on numerical experiments, and guided by the experimental results reported in [28] and in this study, the following capacitance change expression is adopted,

$$\Delta C = C_0 - C = \epsilon_0 \epsilon_r w_e \left(\frac{T}{D} - \frac{t}{d} \right) q \left(\frac{U}{D} \right)^\gamma, \quad (7)$$

where the $q(U/D)^\gamma$ term is introduced as a modification to the parallel plate capacitance change term constituting the remainder of Eq. (7). As will become apparent later on, the parameters q and γ are obtained through model comparisons to experiments. Also in the above capacitance change equation, w_e is the electrode width, T and t are the initial and current electrode thickness, D and d are the initial and current electrode gap and U is the level of applied sensor layer compression.

The current distance d between the electrodes as well as their current thickness t depend on the level of layer compression U/H . The current electrode gap d can easily be obtained using the analytical layer model assuming that the conducting layers simply follow the layer deformation predicted by the analytical model. Thus, the following expressions are obtained,

$$d = D + 2u_1(x_1 = D/2, x_2 = S), \quad (8)$$

where d is the current distance between the conducting electrode layers, D is their initial spacing, S is the initial vertical position of the center of the electrode layer, and $u_1(x_1 = D/2, x_2 = S)$ is the horizontal displacement component predicted by the analytical model at the specified electrode center location. Consistent with the analytical model, the above equation takes the form,

$$d = Df(S). \quad (9)$$

In determining the thinning of the electrode layer during layer compression, one must solve a non-trivial heterogeneous elasticity problem under large deformation conditions. While such an effort may be undertaken in future studies, in this work we adapt a simplified approximate layer thinning model that accounts for the proximity of the electrode end to the symmetry plane as well as for the level of layer compression U/H . More specifically, informed by related finite element studies, a minimum t_{min} is used as an asymptotic value for the maximum electrode layer thinning. Thus, in this approximate model, the current layer thickness t is given by,

$$t = t_{min} + (T - t_{min}) e^{-n \frac{U}{H}}, \quad (10)$$

where T is the initial electrode thickness as shown in Fig. 2, t_{min} is as discussed above, n is a constant controlling the electrode thinning rate with respect to the layer compression U/H which as will be shown later on depends on the electrode gap D .

TABLE II

MODEL PARAMETERS FOR THREE DIFFERENT SENSOR GEOMETRIES CONSIDERED IN THIS STUDY. THE PARAMETERS ARE OBTAINED THROUGH CALIBRATION PROCESSES USING EXPERIMENTAL DATA REPORTED IN SEC. IV

$D(\mu\text{m})$	ζ	m	t_{min}/T	n	q	γ
20	20	1	0.7	25	1.85	-0.4
50	20	1	0.7	10	2.65	-0.3
100	20	1	0.7	5	0.65	-0.3

D. On the Model Constants

Using linear theory and a rule of mixtures approach, the electrode layer thinning asymptotes to about 70% of its original thickness at U/H levels of about 50%, assuming its elastic modulus is approximately twice as high as the surrounding dielectric layer. Thus, in this study a $t_{min} = 0.7H$ is adopted.

Furthermore, careful examination of the mechanics of the compressed sensor layer suggests that higher pressures develop in the region closer to the symmetry plane compared to regions located away from the symmetry plane. In addition, the region closer to the symmetry plane experiences a much faster growth in pressure with increasing U/H compared to regions located further away. These observations may suggest that electrodes placed closer to the symmetry plane should experience larger and more rapid thinning with U/H compared to those placed further away from the symmetry plane. As a result, the constant n appearing in (10) should increase as the electrode spacing, D decreases. Through numerical experiments and model calibration studies involving sensor capacitance-contact force data, the exponent n was determined to be $n = 25$ for $D = 20 \mu\text{m}$, $n = 10$ for $D = 50 \mu\text{m}$, and $n = 5$ for $D = 100 \mu\text{m}$.

A more complete discussion on the calibration of the capacitance model presented above is included later on in this study as part of the model comparisons to the reported experimental results. However, for completeness, all model variables, i.e., ζ , m , n , q , and γ obtained through the model calibration studies for each of the three sensors tested, are reported in Table II.

To summarize the model, the sensor capacitance change ΔC , Eq. (7), can be expressed in terms of the current electrode spacing d and overlapped area $A = t \times w_e$ as follows,

$$\Delta C(U) = \varepsilon_0 \varepsilon_r w_e \left(\frac{T}{D} - \frac{t(U)}{d(U)} \right) q \left(\frac{U}{D} \right)^\gamma, \quad (11)$$

where $d(U)$ and $t(U)$ indicate the dependency of the electrode spacing and thickness on the applied displacement U and are found from Eqs. (9) and (10), respectively. When invoking the force-displacement relationship developed in Sec. II-B, the capacitance change can then be expressed in terms of the total contact force as follows,

$$\Delta C(F) = \varepsilon_0 \varepsilon_r w_e \left(\frac{T}{D} - \frac{t(F)}{d(F)} \right) q \left(\frac{U}{D} \right)^\gamma. \quad (12)$$

The above equation can now be used to carry out parametric studies aiming at investigating critical sensor design aspects such as the initial layer thickness, electrode spacing and

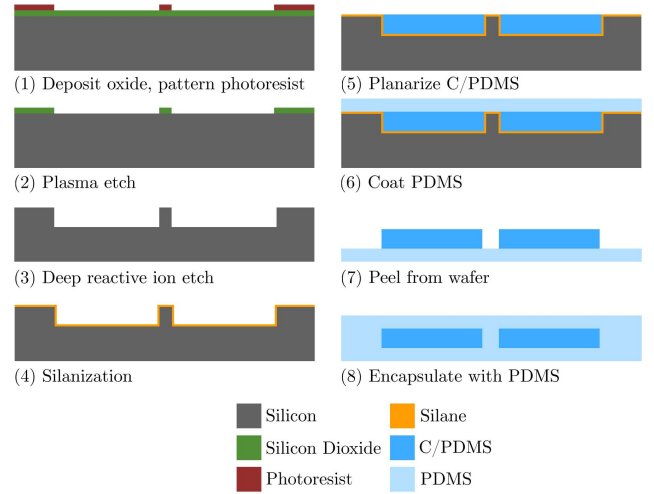


Fig. 4. Microfabrication process used to create all-elastomer in-plane capacitors.

electrode depth as needed for the optimal design of the sensor for different applications. Profiles of ΔC plotted against the applied force as predicted by the above model equation are reported in subsequent sections of this study.

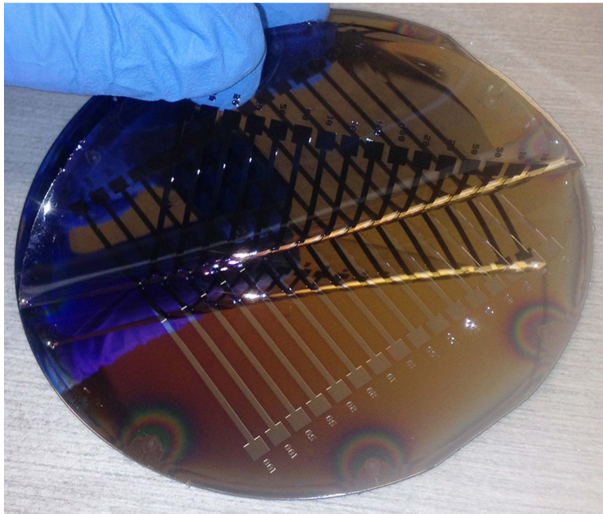
III. EXPERIMENTAL METHODS

To validate this mechanics model for soft tactile sensors, the sensors are fabricated using a variation on the micromolding process first reported in [28]. A test setup seen in Fig. 7 was used to capture capacitance and force measurements for known displacements to compare with the output of the mechanics model.

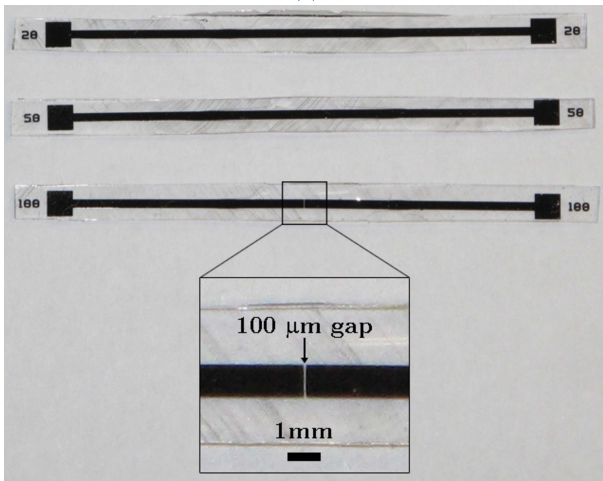
A. Microfabrication

A simple and rapid microfabrication process was used to create the all-elastomer normal force sensors as shown in Fig. 4. Polydimethylsiloxane (PDMS) was selected as the bulk sensor material due to its low modulus to improve force sensitivity, as shown in the developed model. To create the mold, silicon dioxide was deposited on a silicon wafer, and patterned. The bulk silicon was then etched $100 \mu\text{m}$ using a deep reactive ion etch (DRIE). The mold was placed in a desiccator along with $20 \mu\text{L}$ of trichlorosilane (448931, Sigma Aldrich) for 4 hours to silanize the wafer surface [38] and complete the reusable mold.

10 wt. % carbon-polydimethylsiloxane (C/PDMS) was prepared by mixing carbon black powder (39724, Alfa Aesar), 10:1 base-to-curing ratio PDMS (Sylgard 184, Dow Corning), and hexane for 30 min. It was poured on the mold, vacuumed for 2 min at 1 Torr, planarized by hand using an industrial screen printing squeegee (Ryonet), and cured on a hot plate for 15 min at 120°C . After curing, a layer of PDMS was poured on the mold, vacuumed for 15 min at 1 Torr, and cured on a hot plate for 15 min at 120°C . This resulted in a PDMS layer thickness of $500 \mu\text{m}$. The elastomeric sensor was then peeled from the wafer as one whole piece. The sensing area was encapsulated in another layer of PDMS using



(a)



(b)

Fig. 5. (a) Peeling of the fabricated sensors from silicon mold, (b) fabricated sensors for 3 different geometries considered in this study i.e., sensors with electrode gap $D = 20 \mu\text{m}$, $D = 50 \mu\text{m}$, and $D = 100 \mu\text{m}$ as indicated.

the aforementioned process to complete the sensor. The total sensor thickness was $950 \mu\text{m}$.

B. Dimensions of Fabricated Sensors

A typical sensor geometry of the tactile sensors depicted in Fig. 5 is shown in the schematic in Fig. 6. The above schematic includes the 3-D details of the sensor geometry. For illustrative purposes only the right symmetric half of the sensor is shown. In accordance with the microfabrication process presented earlier in this work, the total thickness of the sensors was $H = 950 \mu\text{m}$ while the dielectric layer width was $w_d = 3,500 \mu\text{m}$. Electrode layers of initial thickness $T = 100 \mu\text{m}$ were placed at $S = 550 \mu\text{m}$ from the bottom sensor surface resulting in a sensor dielectric/electrode/dielectric layered morphology of $500/100/350 \mu\text{m}$. Sensors with electrode gaps of 20 , 50 , and $100 \mu\text{m}$ were fabricated. It may be of importance to note that in these sensors, the electrode width was kept to $1,000 \mu\text{m}$ resulting in a fully embedded electrode sensor morphology. Table III summarizes the dimensions of fabricated sensors. Material testing of these tactile sensors

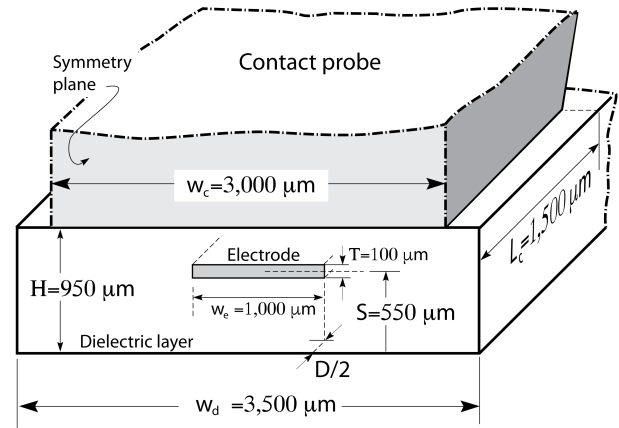


Fig. 6. A schematic showing an isometric view of the symmetric right half of a normal force sensor used in obtaining the experimental data reported in this study.

TABLE III
SUMMARY OF DIMENSIONS OF SENSORS FABRICATED AND TESTED IN THIS STUDY

$H(\mu\text{m})$	$w_d(\mu\text{m})$	$w_e(\mu\text{m})$	$T(\mu\text{m})$	$S(\mu\text{m})$	$D(\mu\text{m})$
950	3,500	1,000	100	550	20
					50
					100

yielded a Modulus of Elasticity $E_d = 1.2 \text{ MPa}$, for the polymer dielectric layer and that of the composite elastomeric electrode to be $E_e = 2.1 \text{ MPa}$.

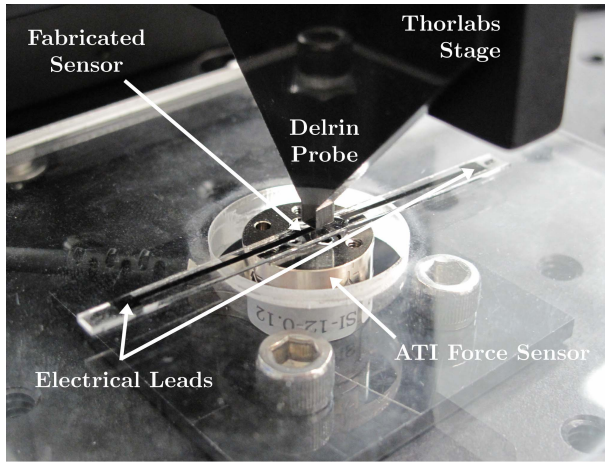
C. Test Setup

Testing was conducted by applying a controlled displacement to the sensor and reading the capacitance and resultant forces. Micron-scale displacements were applied using a Thorlabs PT3-Z8 3-axis stage equipped with a laser cut delrin probe which had a square probe tip area of $3 \times 3 \text{ mm}^2$ consistent with the schematic shown in Fig. 6. Capacitance was measured using an AD7745/46 evaluation board with an observed resolution of 0.1 fF at a sampling rate of 16 Hz ; it was interfaced with the electrical leads to read capacitance. Forces were acquired using an ATI Nano17 6-axis force/torque sensor, and the assembled test setup can be seen in Fig. 7 (a).

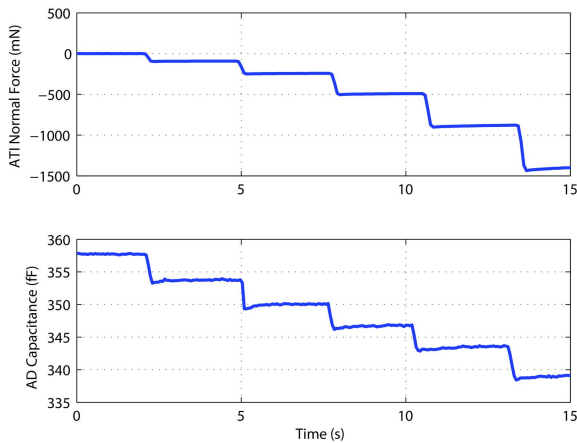
IV. RESULTS

A. Capacitance and Force Results

A displacement was applied normal to the electrode gap for three sensors with initial gaps, $20 \mu\text{m}$, $50 \mu\text{m}$, and $100 \mu\text{m}$, to assess each sensor's performance. Increments of $20 \mu\text{m}$ normal displacement were applied to each sensor up to $100 \mu\text{m}$ (corresponding to a $U/H = 0.105$). Five trials for each sensor were conducted. Sample raw data obtained during normal testing from the ATI sensor and AD board exhibited a step-like behavior in the time domain, Fig. 7(b), and the median value over each step was used for analysis. Post-processed data showing capacitance change plotted against the resultant normal force are shown in Fig. 8. The $20 \mu\text{m}$ gap sensor was found to have the highest sensitivity as expected. At higher



(a)



(b)

Fig. 7. (a) A Thorlabs stage applied a normal displacement to the fabricated sensor via a laser cut delrin probe. An ATI Nano17 force sensor was used to collect resultant forces, and an AD7745/46 evaluation board (not pictured) was interfaced with the electrical leads to read capacitance. (b) Sample raw data during normal testing from the ATI sensor and AD board. Steps are increments of $20 \mu\text{m}$ normal displacements.

normal displacements, a decrease in sensitivity was observed in each sensor as the material saturated under increased compression.

B. Hysteresis Results

Cyclic loading of approximately 2250 mN of normal force was applied to the $20 \mu\text{m}$ gap sensor, Fig. 9. Testing was conducted by displacing the probe $25 \mu\text{m}$ into the sensor then pausing for 1s, and repeating until $150 \mu\text{m}$. Unloading was done in the same manner. This cycling process was carried out for 10 cycles, and each cycle took about 12 s. While testing, the pauses were necessary to sync capacitance and force data during post-processing.

The first cycle had a different loading curve than the remainder of cycles, as described by the Mullins effect [39], while after the sixth cycle the overall behavior followed a consistent path. Around 750 mN, the loading and unloading curves crossed indicating two distinct hysteresis domains. In the sub 750 mN domain, the unloading curve was above

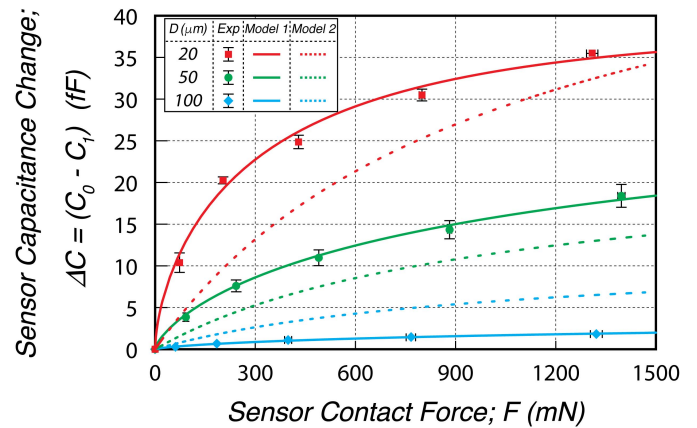


Fig. 8. Change in capacitance as a function of applied normal force for flat plate capacitors of various dielectric gaps. Standard deviations are computed for five trials of the same sensor. The points represent experimental data presented in Sec. IV-A. Model 1 predictions include both the parallel plate and fringe field effects as captured by Eq. (12). Model 2 predictions (dashed lines) represent the capacitance change captured by the parallel plate model only i.e., $\gamma = 0$ and $q = 1$ in Eq. (12).

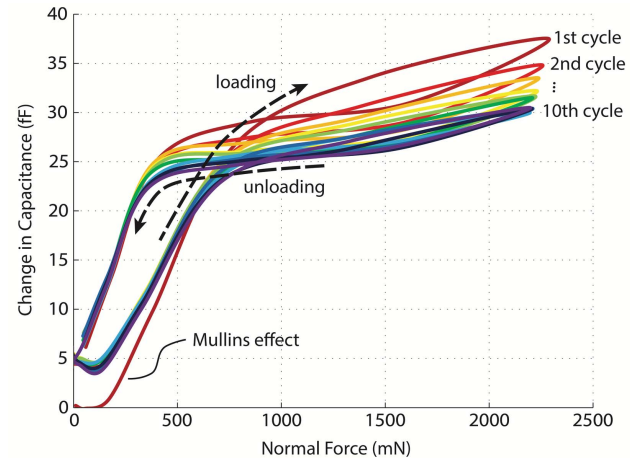


Fig. 9. Hysteresis data obtained by applying cyclic loading of approximately 2250 mN of normal force to the $20 \mu\text{m}$ gap sensor.

the loading curve which may be due to a larger dielectric gap during unloading. Above 750 mN, the unloading curve was below the loading curve which may be due to a smaller electrode height during unloading. The observed hysteretic behavior, similar to human skin, could be accounted for in a robotic system [40].

C. Model Predictions and Comparison to Experiments

In this study, the experimental results reported above are compared with the capacitance predictions obtained using the non-linear model developed in Sec. II. It is important to note that while experimental elastic moduli values of the dielectric and electrode materials were found, the M-R constants C_1 and C_2 employed by the model were not directly available. Instead, C_1 and C_2 were estimated assuming material incompressibility, i.e., $\nu = 0.5$ while setting the shear modulus given by the two M-R constants as follows,

$$C_1 - C_2 = G = \frac{E}{2(1 + \nu)} = \frac{E}{3}. \quad (13)$$

Therefore, the two M-R constants can be obtained from one another through the measured Elastic Modulus E as follows,

$$C_1 = C_2 + \frac{E}{3}. \quad (14)$$

Consistent with the fabricated sensors, the model uses the sensor geometry variables presented in Table III and Fig. 6. Furthermore, the half-length of the contact probe was set to be $L_c = 1500 \mu\text{m}$ with the contact width $w_c = 3000 \mu\text{m}$. Model simulations are presented for sensors with electrode layer gap of $D = 20, 50,$ and $100 \mu\text{m}$. Model dielectric constants of $\epsilon_0 = 8.8541 \text{ pF/m}$ and $\epsilon_r = 2.4$ are consistent with reported values for Sylgard 184 PDMS [41]. In addition, model predictions were obtained for layer modulus varying in a range $1 \text{ MPa} \leq E \leq 4.0 \text{ MPa}$ thus encompassing the measured value of 1.2 MPa .

As discussed earlier in Sec. II-D, the parameters n and t_{min} were assigned the values listed in Table II for each sensor tested. All other model parameters i.e., ζ, m, q, γ are obtained through a best-fit optimization process in two steps.

In the first step, a refined 4-dimensional grid of $101 \times 11 \times 21 \times 51$ points corresponding to linear distributions in the ranges $0 \leq \zeta \leq 50$, $0.5 \leq m \leq 1.5$, $0 \leq q \leq 3$, and $-1 \leq \gamma \leq 1$ was generated as needed to calibrate the model for each individual sensor. Estimates for the capacitance change and associated applied force were then developed at each grid point with the aid of the analytical capacitance model. With the above solutions at hand, the difference, d_f between the reported experimental data and the associated model predictions was calculated leading to an error estimate function consisting of the sums of the squares of the differences at each available experimental data point. Thus the error function used for best fit estimates was of the form,

$$\begin{aligned} \Psi &= \sum_{p=1}^{n_{exp}} \sum_{i=1}^{n_{\zeta}} \sum_{j=1}^{n_m} \sum_{k=1}^{n_q} \sum_{l=1}^{n_{\gamma}} (d_f^{i,j,k,l,p})^2 \\ &= \sum_{p=1}^{n_{exp}} \sum_{i=1}^{n_{\zeta}} \sum_{j=1}^{n_m} \sum_{k=1}^{n_q} \sum_{l=1}^{n_{\gamma}} (\Delta C_{i,j,k,l}^{model}(F_p) - \Delta C^{exp}(F_p))^2, \end{aligned} \quad (15)$$

where n_{exp} is the number of available experimental data points, $n_{\zeta}, n_m, n_q,$ and n_{γ} are the number of discretized points along the $\zeta, m, q,$ and γ axes respectively.

In the second step, which aims at calibrating the model using experimental data obtained from multiple sensors of different electrode gap, the constants ζ and m were fixed to those values obtained from step 1 i.e., 20 and 1, respectively then a 2-dimensional grid of 151×101 points for $0 \leq q \leq 3$ and $-1 \leq \gamma \leq 1$ was generated and the model was optimized for each individual electrode gap reported in Sec. IV to obtain the fringe field calibration factors, q and γ . A summary of all obtained parameters is presented in Table II.

A three dimensional plot of the above error function for a sensor with an electrode gap of $20 \mu\text{m}$ is shown in Fig. 10(a) while 2D contours are shown in Fig. 10(b). The aforementioned figures are obtained for fixed $\zeta = 20$ and $m = 1$. As shown, the error function, Ψ exhibits a smooth profile in

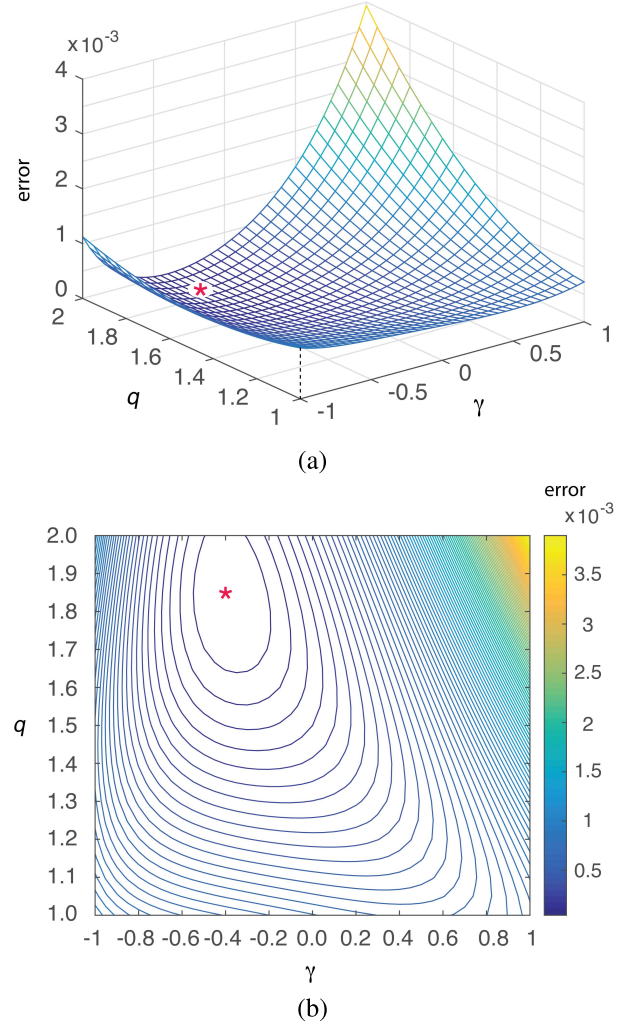


Fig. 10. Plots of the error function Ψ given by Eq. (15) employed in the constrained optimization procedure aimed at best fitting the model predictions to the experimental data presented in Sec. IV. The above figures are obtained for sensor geometry with electrode gap $D = 20 \mu\text{m}$ at fixed parameters $\zeta = 20$ and $m = 1$ for $q - \gamma$ space. (a) The error function Ψ plotted in 3D, (b) 2D contours of the same error function.

the entire q, γ domain used in the study. The model constant values reported in Table II minimize the objective function leading to minimum error estimates and thus best fit results.

The model predictions for the above optimal calibration factors, q, γ , plotted along with the experimental data is shown in Fig. 8 (Model 1). Furthermore, for comparison purposes, the results obtained using parallel plate model alone, without fringe field effects are also shown in the same figure. More specifically, the reported curves obtained using Model 1 are obtained using Eq. (12) with q and γ set at values obtained through optimization process and reported in Table II. On the other hand, the dashed lines are obtained using Eq. (12) but by setting q and γ to 1 and 0, respectively as needed to limit its effect to the parallel plate model. As shown, the parallel plate model underestimates the capacitance change for the $20 \mu\text{m}$ and $50 \mu\text{m}$ gap sensors, while overestimating the capacitance change for the $100 \mu\text{m}$ gap sensor. This effect may be due to a number of reasons primarily related to the deformation of the conducting electrodes. Exceptional agreement is shown

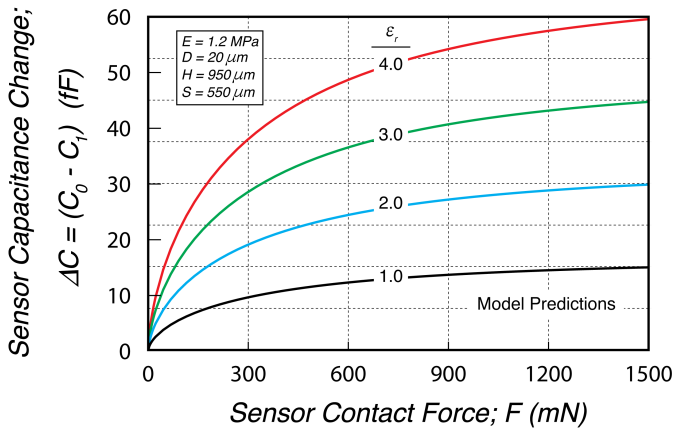


Fig. 11. Model predictions of Sensor Capacitance Change (ΔC) plotted against the predicted sensor contact force (F). This parametric study with four different dielectric layer constants, i.e., $\epsilon_r = 1.0, 2.0, 3.0, 4.0$ as indicated above, was carried out using the sensor geometry show in in Fig. 3, with electrode layer gap $D = 20 \mu\text{m}$, dielectric modulus $E = 1.2 \text{ MPa}$, and calibration factors $q = 1.85, \gamma = -0.4$.

to exist between the analytical model (Model 1, with fringe field effects) predictions and the related experimental data. It is noteworthy that the non-linear model developed herein captures the sensor response over the entire applied force envelope. These findings suggest that the current non-linear sensor capacitance model represents a dramatic improvement over existing linear models [28] and that it can be used to predict the sensor response over its entire sensing range.

D. Parametric Studies

Additional parametric studies were conducted by studying the effects of both the modulus E and constant ϵ_r on the capacitance change, applied force relationship. Fig. 11 includes parametric studies wherein the modulus E was kept constant but ϵ_r was varied. More specifically, Fig. 11 includes simulation predictions for a layer of modulus $E = 1.2 \text{ MPa}$ for the sensor geometry discussed earlier and electrode layer gap equal to $D = 20 \mu\text{m}$. Simulation predictions for $\epsilon_r = 1, 2, 3$ and 4 are presented. As expected, higher capacitance change associated with increased sensor sensitivity is predicted with increasing ϵ_r . Although not reported herein, similar trends in capacitance change were obtained by related simulations for sensors of $50 \mu\text{m}$ and $100 \mu\text{m}$ gap.

In further exploring the modulus effects, simulation results for $D = 20 \mu\text{m}$, $\epsilon_r = 2.4$ and E varying from 1.0 MPa to 4.0 MPa are reported in Fig. 12. These results assume $D = 20 \mu\text{m}$, $H = 950 \mu\text{m}$, $T = 100 \mu\text{m}$, and $S = 550 \mu\text{m}$ in the sensor geometry shown in Fig. 2. A probe/sensor contact area of $3 \times 3 \text{ mm}$ is also assumed. In additions, the results reported in Fig. 12 were plotted with best-fit pair of calibration factors for $D = 20 \mu\text{m}$ i.e., $q = 1.85$, and $\gamma = -0.4$. Four different curves are reported, each corresponding to different dielectric material modulus E as indicated in the figure. As shown, all simulation results show a rapid increase in ΔC at low applied force levels. At higher contact forces, the change in capacitance is predicted to increase less rapidly possibly tending to an asymptote at sufficiently high

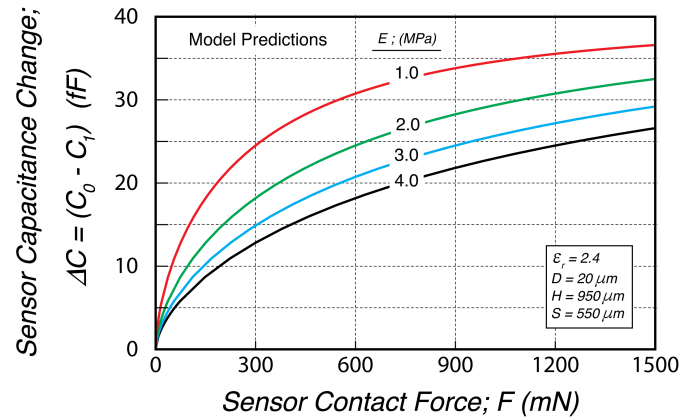


Fig. 12. Model predictions of Sensor Capacitance Change (ΔC) plotted against the predicted sensor contact force (F). This parametric study with different dielectric layer moduli, i.e., $E = 1.0, 2.0, 3.0, 4.0 \text{ MPa}$ as indicated above, was carried out using the sensor geometry show in in Fig. 3, with electrode layer gap $D = 20 \mu\text{m}$, dielectric constant $\epsilon_r = 2.4$, and calibration factors $q = 1.85, \gamma = -0.4$.

values of applied force. As shown, sensors fabricated using elastomeric layers of higher stiffness exhibit less capacitance change with the applied force which indicates a reduction in sensor sensitivity. On the contrary, the results suggest that more compliant sensors, i.e., sensors made with with low modulus E elastomeric layers are predicted to exhibit higher sensitivity in capacitance change with the applied force.

The calibrated model for best fit of all experimental data reported in Sec. IV-C can now be used to better understand the effect of sensor geometry on performance. For this instance, for the best fit pair of $q = 1.85$ and $\gamma = -0.4$ for $D = 20 \mu\text{m}$, the model was used to investigate the effects of electrode layer location. In doing so, the electrode layer position is parameterized by the normalized distance $S = x_2^d/H$, where x_2^d is the distance of the mid-plane of the electrode layer from the bottom of the sensor. The results for four different layer depths are shown in Fig. 13. As shown, higher capacitance change with the applied force is predicted for sensors with electrode layers placed closer to the top surface. This outcome is consistent with the layer mechanics since material points closer to the top surface experience larger u_1 deformations.

Furthermore, the effects of electrode layer thickness on the capacitance are explored by conducting a parametric study wherein the initial thickness T is taken to be $50 \mu\text{m}$, $100 \mu\text{m}$, $125 \mu\text{m}$, $150 \mu\text{m}$. As before, parametric studies are carried out for sensor with a $20 \mu\text{m}$ initial gap. The results of the latter parametric study are reported in Fig. 14. As shown, higher capacitance change is predicted for thicker electrodes.

Finally, Fig. 15 explores the effect of electrode gap, D , on the sensor capacitance change, ΔC , for different electrode thicknesses at fixed $U/H = 30\%$. Sensors with smaller electrode gap and thicker electrodes demonstrate greater sensitivity. This ratio is related to the aspect ratio limitation of the deep reactive ion etch during mold creation. In the above studies, n was interpolated as needed, between the values reported in Table II.

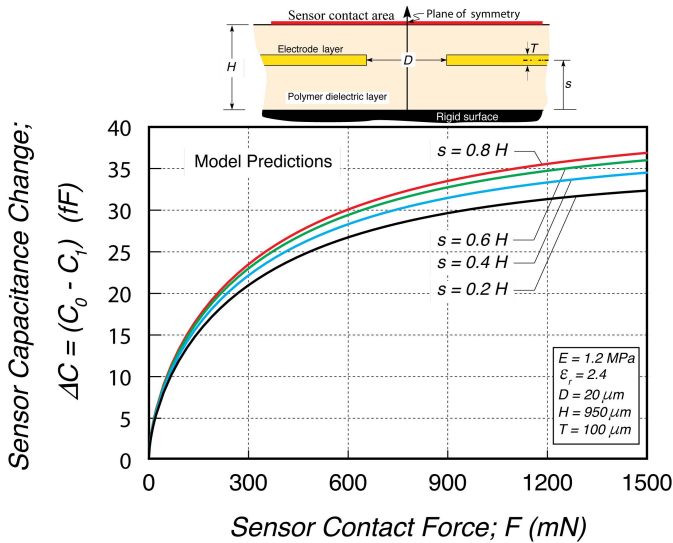


Fig. 13. A parametric study showing the effects of the electrode layer position on the sensor capacitance change with the applied contact force. The reported results were obtained using the predictive capacitance model change developed in this work. The sensor geometry and material parameters used are those included in the figure. The best-fit pair of $q = 1.85$, and $\gamma = -0.4$ was used to plot the above figure. The four different curves represent sensors with the electrode layer placed at different locations along the dielectric layer height as indicated by the electrode layer center position $S = 0.2H, 0.4H, 0.6H, 0.8H$.

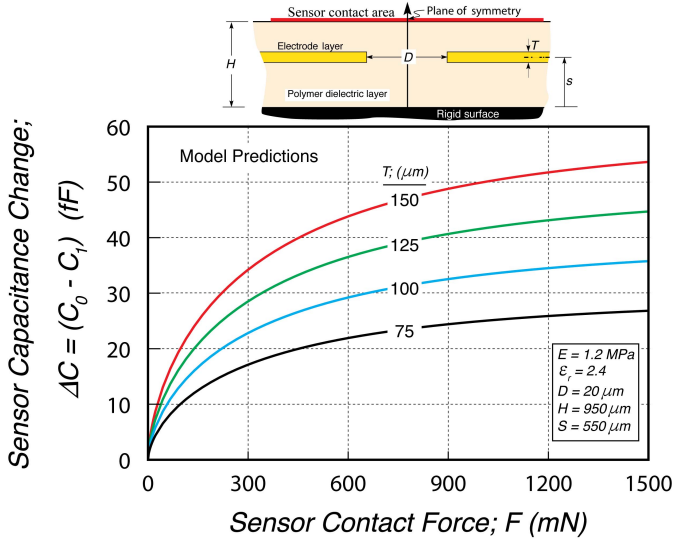


Fig. 14. A parametric study showing the effects of the electrode layer thickness on the sensor capacitance change with the applied contact force. As in Fig. 13, the reported results were obtained using the predictive capacitance model change developed in this work. The sensor geometry and material parameters used are those included in the figure with the electrode layer mid-plane place at $S = 550$ μm . The best-fit pair of $q = 1.85$, and $\gamma = -0.4$ was used to plot the above figure. Results for four different electrode thicknesses are reported, i.e., $T = 0.08H, 0.11H, 0.13H, 0.16H$.

V. DISCUSSION

The capacitance model developed in this work employs a non-linear mechanics model capable of predicting the deformations induced in the soft elastomeric sensor layer during contact. Thus, layer deformation under modest as well as severe contact conditions can be captured. As a result, the capacitance model built on parallel plate capacitance theory and augmented to include fringe field effects, has been

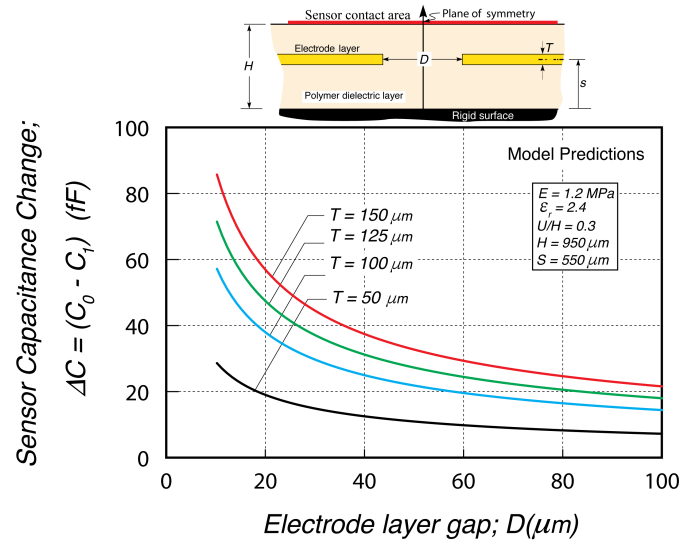


Fig. 15. A parametric study aimed at exploring the effects of electrode gap D and electrode layer thickness T . As before, the results were obtained using the capacitance model developed in this study. The sensor geometry is consistent with Fig. 3 and related sensor parameters including the material properties used are reported in the figure. The different curves correspond to different electrode layer thicknesses $T = 50, 100, 125$, and 150 μm for the sensors subjected to the same contact force $F = 568.8$ mN, corresponding to top sensor compressive deformation $U/H = 0.3$.

demonstrated to capture the sensor response for both small as well as large contact loads spanning three orders of magnitude from mN to several N of applied force. Through the reported model predictions, parametric studies, and comparisons to experiments, several observations can be made and relevant questions can be asked. For example, the model calibration studies guided by experimental sensor capacitance data have shown that the overall capacitance model predictions match impressively closely the data for all three sensors fabricated in this study. However, the fringe field calibration factors, q and γ , obtained through an optimization process have been shown to be dependent on sensor geometry, more specifically the gap between electrodes. As discussed in more detail in Sec. II-C, this observation is consistent with fringe field theories.

The reported parametric studies exploring the effects of material and electrode layer properties as well as the effects of sensor geometry design, i.e., the effects of sensor layer thickness, electrode layer thickness and depth and electrode layer gap, provide useful insights for the design of tactile sensors with enhanced capacitance sensitivity. More specifically, sensors built using softer elastomers are shown to have increased capacitance change sensitivity. Similarly, sensors with small electrode layer gap are also shown to exhibit higher capacitance change sensitivity. In addition, it has been shown that the sensitivity increases for sensors with electrode layers placed closer to the top surface. Although sensor design limitations may arise due to microfabrication constraints and material availability, the non-linear capacitance model developed in this work provides useful guidelines for the optimal design of such tactile sensors.

In addition, geometric characterization of the fabricated tactile sensor may be needed in order to establish with confidence

the final sensor geometry as it compares to the sensor design geometry. Small deviations from the design dimensions may have an effect on the sensor performance and may lead to further deviations from the model predictions. Finally, additional experiments testing sensors of different electrode layer gap, layer thickness and layer depth can be used to increase confidence in the predictive capabilities of the model. The model can then be used to establish design guidelines for tactile sensors with this geometry accompanied by the relevant multi-step micro-fabrication process, thus advancing the development of flexible, all elastomer, in-plane MEMS tactile sensors.

In summary, the model parametric studies suggest greater capacitance force sensitivity is obtained for sensors designed with smaller electrode gap, smaller overall thickness, electrode layer placed closer to the top surface, softer dielectric layer material, and thicker electrode. It may be noteworthy to mention that one may arrive at many of the above findings on optimal sensor design using a first order linear model. However, the current non-linear model allows for sensible quantification of the effects of each sensor parameter, including electrode depth and sensor thickness while offering for the first time the ability to capture the force capacitance change over the entire applied force regime.

It may be of importance to note that while the current pressure sensor model has been shown to accurately predict the applied force-capacitance change over the entire sensing regime, the model is also capable of returning sensor strain estimates. Such sensor strain predictions would however be limited to deformation events that are consistent with the applied pressure loading modeled by the large deformation, large strain mechanics presented in [34] and used in the development of the sensor model. This would limit the use of the current sensor model in applications involving surrounding strain changes to a few special cases wherein the sensor is attached to adjacent surfaces experiencing differential normal displacements. In order to develop a more robust sensor capable of functioning as a multidirectional strain gage, the current model will need to be expanded to include the combined application of normal loads on both sensor directions and potentially in-plane and out-of-plane shear loads. In fact this topic is the focus of on-going studies and shall be addressed in future works.

VI. CONCLUSIONS

A predictive non-linear capacitance change model has been developed for tactile capacitance sensors subjected to pressure loading. This new model expands existing linear model capabilities and can be used to predict the sensor response over its entire sensing range. The model incorporates the non-linear deformation mechanics for a soft elastomeric layer subjected to uniform compressive displacement condition. The model was properly adjusted to incorporate the finite contact probe effects through a rigorous shear stress integration technique. The capacitance change model was embedded into an optimization algorithm aimed at identifying model parameters that resulted in best fit model predictions with reported experimental data for three self-similar sensor systems. The calibrated

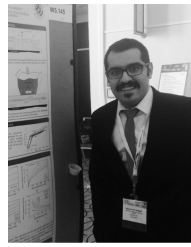
model predictions were shown to be in excellent agreement with the experimental results over the entire applied force range for all three sensors tested.

The model capabilities were further explored by conducting broad parametric studies aimed at investigating the effects of layer modulus, electrode layer properties, electrode layer location and thickness as well as the effects of electrode layer gap. The outcomes suggest that the current capacitance model has broad predictive capabilities that may assist in the optimal design of related all-elastomer MEMS tactile sensors. More specifically, in accordance with the model predictions, the capacitance change sensitivity of an all elastomer tactile sensor increases by, 1) decreasing the electrode layer spacing/gap D , 2) by increasing the electrode layer thickness T , 3) by placing the electrode layers as close to the sensor surface as possible, 4) by using soft elastomeric layer material of as low modulus as possible and 5) by minimizing the sensor thickness H as needed to achieve higher U/H levels during contact.

REFERENCES

- [1] S. C. Jacobsen, I. D. McGammon, K. B. Biggers, and R. P. Phillips, "Design of tactile sensing systems for dextrous manipulators," *IEEE Control Syst. Mag.*, vol. 8, no. 1, pp. 3–13, Feb. 1988.
- [2] R. S. Dahiya, G. Metta, M. Valle, and G. Sandini, "Tactile sensing—From humans to humanoids," *IEEE Trans. Robot.*, vol. 26, no. 1, pp. 1–20, Feb. 2010.
- [3] M. H. Lee and H. R. Nicholls, "Review article tactile sensing for mechatronics—A state of the art survey," *Mechatronics*, vol. 9, no. 1, pp. 1–31, Feb. 1999.
- [4] H. Yousef, M. Boukallel, and K. Althoefer, "Tactile sensing for dexterous in-hand manipulation in robotics—A review," *Sens. Actuators A, Phys.*, vol. 167, no. 2, pp. 171–187, Jun. 2011.
- [5] G. Ursini *et al.*, "Stress-related methylation of the catechol-O-methyltransferase Val 158 allele predicts human prefrontal cognition and activity," *J. Neurosci.*, vol. 31, no. 18, pp. 6692–6698, May 2011.
- [6] S. Haddadin, A. Albu-Schaffer, M. Strohmayer, M. Frommberger, and G. Hirzinger, "Injury evaluation of human-robot impacts," in *Proc. IEEE Int. Conf. Robot. Autom. (ICRA)*, May 2008, pp. 2203–2204.
- [7] S. Phan *et al.*, "Capacitive skin sensors for robot impact monitoring," in *Proc. IEEE/RSJ Int. Conf. Intell. Robots Syst. (IROS)*, Sep. 2011, pp. 2992–2997.
- [8] K. Kim *et al.*, "Polymer-based flexible tactile sensor up to 32×32 arrays integrated with interconnection terminals," *Sens. Actuators A, Phys.*, vol. 156, no. 2, pp. 284–291, Dec. 2009.
- [9] J. Engel, J. Chen, Z. Fan, and C. Liu, "Polymer micromachined multimodal tactile sensors," *Sens. Actuators A, Phys.*, vol. 117, no. 1, pp. 50–61, Jan. 2004.
- [10] Tekscan | *Pressure Mapping, Force Measurement, & Tactile Sensors*, accessed on May 2015. [Online]. Available: <https://www.tekscan.com/>
- [11] M. W. Strohmayer, H. P. Saal, A. H. Potdar, and P. van der Smagt, "The DLR touch sensor I: A flexible tactile sensor for robotic hands based on a crossed-wire approach," in *Proc. IEEE/RSJ Int. Conf. Intell. Robots Syst. (IROS)*, Oct. 2010, pp. 897–903.
- [12] L. Ventrelli, L. Beccai, V. Mattoli, A. Menciassi, and P. Dario, "Development of a stretchable skin-like tactile sensor based on polymeric composites," in *Proc. IEEE Int. Conf. Robot. Biomimetics (ROBIO)*, Dec. 2009, pp. 123–128.
- [13] A. P. Gerratt and S. Bergbreiter, "Microfabrication of compliant all-polymer MEMS thermal actuators," *Sens. Actuators A, Phys.*, vol. 177, pp. 16–22, Apr. 2012.
- [14] Y.-L. Park, C. Majidi, R. Kramer, P. Bérard, and R. J. Wood, "Hyperelastic pressure sensing with a liquid-embedded elastomer," *J. Microeng. Microeng.*, vol. 20, no. 12, p. 125029, 2010.
- [15] R. A. Boie, "Capacitive impedance readout tactile image sensor," in *Proc. IEEE Int. Conf. Robot. Autom.*, vol. 1, Mar. 1984, pp. 370–378.
- [16] B. L. Gray and R. S. Fearing, "A surface micromachined microtactile sensor array," in *Proc. IEEE Int. Conf. Robot. Autom.*, vol. 1, Apr. 1996, pp. 1–6.

- [17] K. Chun and K. D. Wise, "A high-performance silicon tactile imager based on a capacitive cell," *IEEE Trans. Electron Devices*, vol. 32, no. 7, pp. 1196–1201, Jul. 1985.
- [18] J. Ulmen and M. Cutkosky, "A robust, low-cost and low-noise artificial skin for human-friendly robots," in *Proc. IEEE Int. Conf. Robot. Autom. (ICRA)*, May 2010, pp. 4836–4841.
- [19] S. P. Lacour and D. P. J. Cotton, "Elastomeric capacitive sensors," in *Proc. 16th Int. Solid-State Sensors, Actuators, Microsyst. Conf. (TRANSDUCERS)*, Jun. 2011, pp. 2770–2773.
- [20] H.-K. Lee, S.-I. Chang, and E. Yoon, "A flexible polymer tactile sensor: Fabrication and modular expandability for large area deployment," *Microelectromech. Syst., J.*, vol. 15, no. 6, pp. 1681–1686, Dec. 2006.
- [21] D. J. Lipomi *et al.*, "Skin-like pressure and strain sensors based on transparent elastic films of carbon nanotubes," *Nature Nanotechnol.*, vol. 6, pp. 788–792, Oct. 2011.
- [22] C.-F. Hu, J.-Y. Wang, Y.-C. Liu, M.-H. Tsai, and W. Fang, "Development of 3D carbon nanotube interdigitated finger electrodes on polymer substrate for flexible capacitive sensor application," *Nanotechnology*, vol. 24, no. 44, pp. 444006–1–444006–14, 2013.
- [23] D. J. Cohen, D. Mitra, K. Peterson, and M. M. Maharbiz, "A highly elastic, capacitive strain gauge based on percolating nanotube networks," *Nano Lett.*, vol. 12, no. 4, pp. 1821–1825, 2012.
- [24] R. D. P. Wong, J. D. Posner, and V. J. Santos, "Flexible microfluidic normal force sensor skin for tactile feedback," *Sens. Actuators A, Phys.*, vol. 179, pp. 62–69, Jun. 2012.
- [25] A. Fassler and C. Majidi, "Soft-matter capacitors and inductors for hyperelastic strain sensing and stretchable electronics," *Smart Mater. Struct.*, vol. 22, no. 5, p. 055023, 2013.
- [26] H.-S. Shin, J. Ryu, C. Majidi, and Y.-L. Park, "Enhanced performance of microfluidic soft pressure sensors with embedded solid microspheres," *J. Micromech. Microeng.*, vol. 26, no. 2, pp. 1–9, Apr. 2016.
- [27] O. A. Araromi *et al.*, "Rollable multisegment dielectric elastomer minimum energy structures for a deployable microsatellite gripper," *IEEE/ASME Trans. Mechatron.*, vol. 20, no. 1, pp. 438–446, Feb. 2015.
- [28] A. Charalambides and S. Bergbreiter, "All-elastomer in-plane MEMS capacitive tactile sensor for normal force detection," in *Proc. IEEE SENSORS*, Nov. 2013, pp. 1–4.
- [29] A. Charalambides and S. Bergbreiter, "A novel all-elastomer MEMS tactile sensor for high dynamic range shear and normal force sensing," *J. Micromech. Microeng.*, vol. 25, no. 9, p. 095009, 2015.
- [30] S. C. B. Mannsfeld *et al.*, "Highly sensitive flexible pressure sensors with microstructured rubber dielectric layers," *Nature Mater.*, vol. 9, pp. 859–864, Sep. 2010.
- [31] Y.-L. Park, B.-R. Chen, and R. J. Wood, "Design and fabrication of soft artificial skin using embedded microchannels and liquid conductors," *IEEE Sensors J.*, vol. 12, no. 8, pp. 2711–2718, Aug. 2012.
- [32] R. S. Fearing, "Tactile sensing mechanisms," *Int. J. Robot. Res.*, vol. 9, no. 3, pp. 3–23, 1990.
- [33] D. A. Kontarinis, J. S. Son, W. Peine, and R. D. Howe, "A tactile shape sensing and display system for teleoperated manipulation," in *Proc. IEEE Int. Conf. Robot. Autom.*, vol. 1, May 1995, pp. 641–646.
- [34] K. M. Kalayeh and P. G. Charalambides, "Large deformation mechanics of a soft elastomeric layer under compressive loading for a MEMS tactile sensor application," *Int. J. Non-Linear Mech.*, vol. 76, pp. 120–134, Nov. 2015.
- [35] L. E. Malvern, *Introduction to the Mechanics of a Continuous Medium*. Englewood Cliffs, NJ, USA: Prentice-Hall, 1969.
- [36] H. B. Palmer, "The capacitance of a parallel-plate capacitor by the Schwartz-Christoffel transformation," *Elect. Eng.*, vol. 56, no. 3, pp. 363–368, Mar. 1937.
- [37] M. Hosseini, G. Zhu, and Y.-A. Peter, "A new formulation of fringing capacitance and its application to the control of parallel-plate electrostatic micro actuators," *Analog Integr. Circuits Signal Process.*, vol. 53, no. 2, pp. 119–128, Dec. 2007.
- [38] P. Kuhn, K. Eyer, S. Allner, D. Lombardi, and P. S. Dittrich, "A microfluidic vesicle screening platform: Monitoring the lipid membrane permeability of tetracyclines," *Anal. Chem.*, vol. 83, no. 23, pp. 8877–8885, 2011.
- [39] L. Mullins, "Softening of rubber by deformation," *Rubber Chem. Technol.*, vol. 42, no. 1, pp. 339–362, Mar. 1969.
- [40] D. M. Siegel, S. M. Drucker, and I. Garabieta, "Performance analysis of a tactile sensor," in *Proc. IEEE Conf. Robot. Autom.*, vol. 4, Mar. 1987, pp. 1493–1499.
- [41] *Sylgard 184 Silicone Elastomer Kit*, accessed on Jan. 2015. [Online]. Available: <http://www.dowcorning.com/applications/search/products/Details.aspx?pro%id=01064291>



Kourosh M. Kalayeh received the B.Sc. degree in material science and engineering from the Amirkabir University of Technology, Tehran, Iran, in 2012. He is currently pursuing the Ph.D. degree in mechanical engineering with the University of Maryland, Baltimore County (UMBC), Baltimore, MD, USA. He is currently with Dr. Charalambides' Computational Fracture Mechanics and Composites Laboratory, UMBC. His research interests include mathematical modeling, numerical simulations, computational mechanics, automatic controls, and MEMS sensors.



Alexi Charalambides received the B.S. and M.S. degrees from the University of Maryland, Baltimore County, in 2009 and 2011, respectively, and the Ph.D. degree from the University of Maryland at College Park in 2016, all in mechanical engineering. He joined the Microrobotics Laboratory, University of Maryland at College Park, in 2013. He is currently a Post-Doctoral Researcher with the Robotics Institute, Carnegie Mellon University.



Sarah Bergbreiter received the B.S.E. degree in electrical engineering from Princeton University in 1999, and the M.S. and Ph.D. degrees from the University of California at Berkeley, Berkeley, in 2004 and 2007, respectively, with a focus on microrobotics. She is currently an Associate Professor of Mechanical Engineering, with a joint appointment at the Institute for Systems Research, University of Maryland at College Park. She received the DARPA Young Faculty Award in 2008, the NSF CAREER Award in 2011, and the Presidential Early Career Award for Scientists and Engineers in 2013 for her research on engineering robotic systems down to sub-millimeter size scales. She was a recipient of the Best Conference Paper Award at the IEEE ICRA 2010 on her work incorporating new materials into microrobotics and the NTF Award at the IEEE IROS 2011 for early demonstrations of jumping microrobots.



Panos G. Charalambides received the B.Sc. degree in civil engineering from the Aristotle University of Thessaloniki, Greece, in 1981, and the M.Sc. and Ph.D. degrees in theoretical and applied mechanics from the University of Illinois at Urbana-Champaign in 1983 and 1986, respectively. During his Post-Doctoral studies with the Department of Materials, University of California at Santa Barbara, he was involved in pioneering studies with several collaborators on the characterization of bimaterial interface fracture. He was with Michigan Technological University from 1989 to 1993, where he received the prestigious NSF sponsored Presidential Young Investigator award. He joined the Department of Mechanical Engineering, the University of Maryland, Baltimore County, in 1994. He served as the Chair of the Department of Mechanical Engineering from 2002 to 2008. He has supervised over 20 M.S. and Ph.D. students and has authored extensively in his area of research.